Evaluating the strength of grade 10.9 bolts subject to multiaxial loading using the micromechanical failure index MCEPS

Xin, Haohui; Li, Jie; Veljkovic, Milan; Liu, Yuqing; Sun, Qing

Important note
To cite this publication, please use the final published version (if applicable).
Please check the document version above.

Haohui Xin, Jie Li, Milan Veljkovic, Yuqing Liu, Qing Sun

ARTICLE

Evaluating the strength of grade 10.9 bolts subject to multiaxial loading using the micromechanical failure index: MCEPS

Bolted joints in steel structures are generally subject to combined actions. The research on ultimate capacity of bolted joints under combined tension and shear actions, twin shear actions, and combined tension-twin shear actions is relatively limited. The aim of this paper is to calibrate the fracture locus of grade 10.9 bolts using the mesoscale critical equivalent plastic strain (MCEPS). We use ductile fracture simulation to numerically evaluate the ultimate resistance of bolts subject to multiaxial loading and compare the results with the current design standards. The results show that predictions for grade 10.9 bolts subject to multiaxial loading in Chinese code GB 50017 and American code AISC-360 are not on the safe side, while predictions in European code EN1993-1-8:2005 are slightly on the conservative side. We propose two modification factors to improve prediction of bolt strength subject to multiaxial loading; namely the multiaxial loading factor for shear resistance ξ_v and the multiaxial loading factor for tensile resistance ξ_t.

Keywords high-strength bolts; ductile fracture; multiaxial loading; ultimate capacity

1 Introduction

High-performance bolts are widely used in structural steel joints combing benefit in high strength, fire resistance and corrosion resistance. with or without a pretension force respectively. When designing bolted connections, it is important to predict the ultimate resistance of bolts subject to multiaxial loading. The axial tensile and pure shear strength have been experimentally and numerically investigated in past decades [1–10]. Nevertheless, bolted joints are generally exposed to combined actions in steel structures applications, including combined tension and shear actions, twin shear actions, and combined tension-twin shear actions. The ultimate strength of grade 10.9 bolts [11], grade 12.9 bolts [12], and stainless bolts [13] under combined tension and shear actions has recently been evaluated. The research on ultimate resistance subject to twin shear loading and combined tension-twin shear loading is limited. In addition, it is relatively difficult to design a set-up to apply twin pure shear loading or triaxial tensile and shear loading to the bolts. Ultimate bolt resistance (Eurocode terminology used) is predicted based on the following two assumptions: the failure occurs in the shank of the bolt and the hole clearance effect is disregarded.

Advances in material modelling in recent years have led to increased confidence in the finite element method as an effective way to predict the ultimate resistance of bolts subject to multiaxial loading. Bolt failure is a progressive material deterioration due to the nucleation, growth, and coalescence of microvoids [14]. The microvoids can be nucleated by either matrix-particle decohesion or particle cracking. After nucleation, the microvoids enlarge due to plastic deformation. Void coalescence by internal necking or shear localization (the two common modes) [15] results in ductile fracture.

Ductile fracture simulation is essential for predicting the ultimate capacity of high-performance bolts. The fracture models generally consist of physically-based [16–23] and phenomenological models [24–32]. McClintock (1968) [16] and Rice & Tracey (1969) [17] improved early physically-based ductile fracture prediction by analyzing the evolution of cylindrical and spherical holes in a ductile matrix. Gurson (1977) [18] proposed a (porous) plasticity model which includes the void volume fraction as an internal variable. Tevergaard and Needleman (1984) [19, 20] proposed the Gurson-Tevergaard-Needleman (GTN) model, an improvement on the original Gurson model which takes account of void coalescence. The GTN model has been further extended to consider anisotropy [21] and shear effects [22, 23]. The physical model assumed that the fracture occurs when the microvoid radius or void volume fraction reaches a critical threshold value. The phenomenological models can be subdivided into the uncoupled damage model and coupled damage model [33]. In terms of the uncoupled phenomenological model [33], the basic assumption is that the evolution of damage does not affect the effective stress-strain response of high strength steels (HSS) before a fracture occurs. Generally, the J2 plasticity model is used in combination with a separate fracture model. It is assumed that the fracture occurs at a point where a weighted measure of the accumulated equivalent plastic strain reaches a critical value [24–26], such as the Johnson-Cook model [27], the MMC model [28], the Hosford-Coulomb model [29, 30], or the Lou-Huh model [31, 32]. The critical equivalent plastic strain at the onset of fracture is the function of the stress triaxiality and the Lode (angle) parameter. In terms of the coupled phenomenological model [33], the irreversible damage process is accounted for by the internal constitutive variables involved in the yield surface [34–36]. Generally, a damage scalar is adopted to describe the isotropic damage, and effective stress is used to describe the impact of the damage on the macro behavior of the materials [36].

The material parameters of the uncoupled phenomenological models were calibrated using a series of material
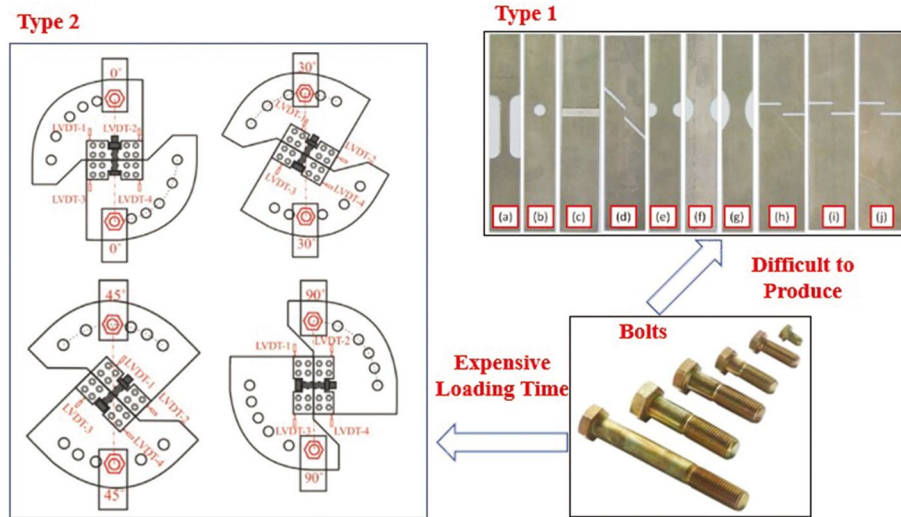
Fig. 1   Illustration of material tests to obtain fracture locus (Type 1 and 2 is reproduced from references [12, 31])

tests. In general, there are two methods to obtain different stress status in terms of stress triaxiality and lode parameter as illustrated in Fig. 1: Type 1 using different geometry; Type 2 using different force combinations. It is difficult to produce the different bolt specimens required to generate the pure tensile stress status, pure shear stress status, plain strain tensile stress status, combined tensile-shear stress statuses etc. Furthermore, it is also time-consuming to make the loading set-up and test a series of bolt specimens using a cycle rig. Hence, the mesoscale computational homogenization generated by the physical model, combined with the uncoupled phenomenological model, offers a promising means of predicting the ductile fracture of HSS from the uniaxial stress-strain relationship alone [37, 38].

The aim of this paper is to calibrate the fracture locus of grade 10.9 bolts based on the mesoscale critical equivalent plastic strain (MCEPS) proposed in [37, 38]. We use the finite element method to simulate numerically the ductile fracture of bolts subject to combined tension-shear actions, twin-shear actions, and combined tension-twin shear actions. Then we compare the ultimate resistance numerically predicted in this paper with the existing design provisions.

2   Ductile fracture locus of bolts

In this paper we divided the process of predicting the ductile fracture of high strength bolts into two stages: 1: Identify the relationship between equivalent plastic strain and uniaxial true stress for the isotropic J2 plasticity model; 2: Identify parameters of fracture strain under multiaxial stress states. It is assumed that the evolution of damage does not affect the uniaxial true stress-strain response of HSS before a fracture occurs. The detailed calibration process is reported in [37, 38].
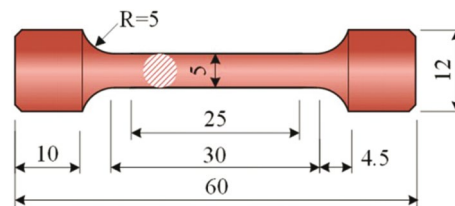
Fig. 2.   Tensile coupon specimens of grade 10.9 bolt [39]
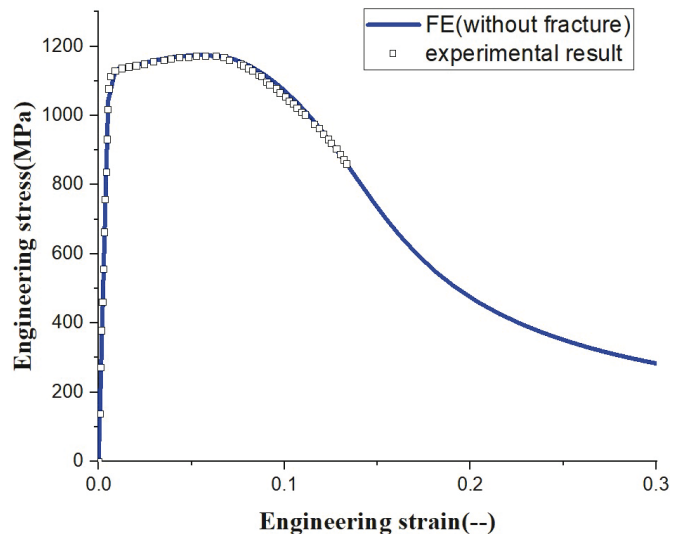
Fig. 3.   Comparisons between FE (without damage) and experimental results (Experimental data is reproduced from [39])

2.1   Specimens

Tensile coupon specimens of grade 10.9 bolts with diameters of 5 mm [39] are used in this paper to calibrate the ductile fracture locus. The geometric dimensions of the specimens are shown in Fig. 2. The test result is shown in Fig. 3.

2.2.   Calibration of plastic flow stress

The whole uniaxial stress-strain relationship is divided into three stages: elastic stage, plastic stage, and coupled

H. Xin, J. Li, M. Veljkovic, Y. Liu, Q. Sun: Evaluating the strength of grade 10.9 bolts subject to multiaxial loading using the micromechanical failure index: MCEPS

ARTICLE

Fig. 4 Finite element model and boundary conditions of bolt specimen

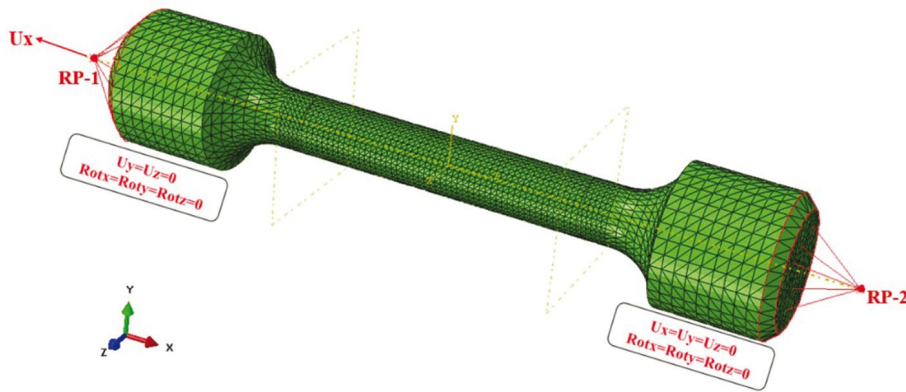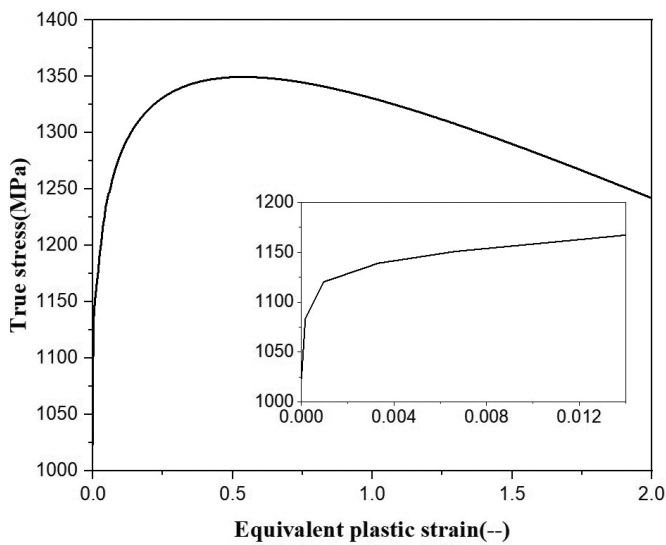**Fig. 5** Uniaxial true stress-strain curves without considering the damage

plastic-damage stage. The coupled plastic-damage stage is further broken down into the plastic-dominated zone and the damage-dominated zone [40]. The finite element (FE) model and boundary conditions used to calibrate the parameters of the coupled plastic-damage stage are shown in Fig. 4. Note that the specimen was simulated by solid element C3D10M with a fixed mesh size of 0.5 mm to avoid mesh size effects on the FE results. One end of the specimen is coupled with reference point RP1 and the

other end is coupled with reference point RP2. All the degrees of freedom of RP1 are fixed, and the loading is applied to RP2 using displacement with remaining degrees of freedom fixed. The quasi-static simulation is utilized through the ABAQUS/EXPLICIT solver with a total time of 1s and a time interval of 5×10^{-5} s for the mass scaling.

The FE simulation is consistent with the experimental results, as shown in Fig. 3. The calibrated parameters for the plastic stage and coupled plastic-damage stage are summarized in Tab. 1. The calibrated uniaxial true stress-strain relationship without considering the damage is shown in Fig. 5.

2.3. Calibration of fracture locus

A mesoscale failure index is generally used to link the material fracture under different multiaxial stress status. The basic assumption is that the critical value of the mesoscale failure index remains constant under multiaxial and non-proportional loading. Based on the authors' previous research, the homogenized value of homogenized equivalent plastic strain $\bar{\varepsilon}^{\mathbf{p}}$ at the microvoid surface Γ_{v} is used [37, 38] as the mesoscale failure index. Fig. 6 shows the mesoscale indicator evolution with increasing equivalent plastic strain. The relationship between strain ratio and fracture strain subject to uniaxial strain is fitted by a seven-term polynomial expression. The fitted coefficients are summarized in Tab. 2.

$$MI = \frac{1}{\left|\Gamma_{\mathrm{v}}\right|} \int_{\Gamma_{\mathrm{v}}} \bar{\varepsilon}^{\mathbf{p}} d\Gamma \qquad (1)$$

$$r_{\chi} = \sum_{i=1}^{7} \xi_i \left(\bar{\varepsilon}_{\mathbf{UT}}^{\mathbf{p}}\right)^{i-1} \quad \chi = "SH/UT","PST/UT" \qquad (2)$$

Tab. 1 Calibrated parameters for coupled plastic-damage stage

$\bar{\sigma}_{\mathbf{u}}$	$\bar{\varepsilon}_{\mathbf{u}}^{\mathbf{p}}$	W	$\bar{\varepsilon}_{\mathbf{d\text{-}1}}^{\mathbf{p}}$	B
(MPa)	(---)	(---)	(---)	(---)
1247.15	0.0592	0.00	0.0681	0.11

Tab. 2 Fitted coefficients of polynomial expression in Eq. (2)

		ξ_1	ξ_2	ξ_3	ξ_4	ξ_5	ξ_6	ξ_7
MI	$r_{\mathrm{SH/UT}}$	−0.4268	1.7349	−2.8124	2.2348	−0.7533	−0.0366	1.0031
	$r_{\mathrm{PST/UT}}$	4.4981	−16.589	23.111	−15.031	4.6355	−0.7718	0.9121
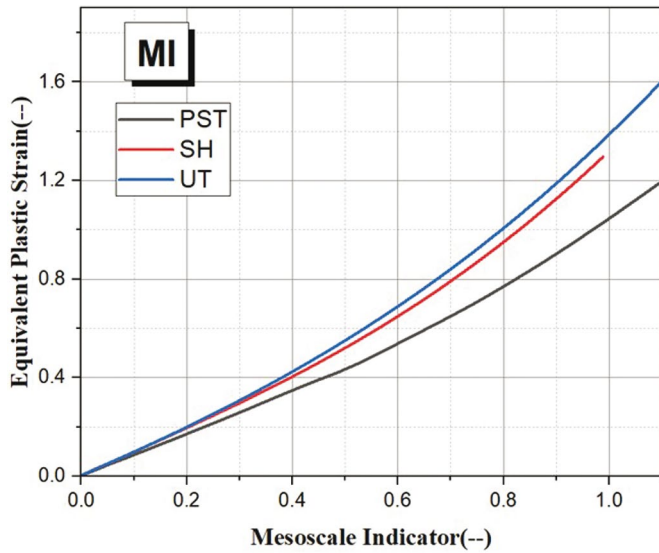
Fig. 6 Mesoscale indicator evolution along with the equivalent plastic strain

Fig. 7 Comparisons between FE simulation and physical test results

Where: UT denotes uniaxial tension stress status; SH denotes the pure shear stress status; PST denotes the plane strain tension stress status.

In this paper, fracture locus (which is a function of stress triaxiality and the Lode parameter) is identified by the Lou-Huh model as expressed in Eq. (3).

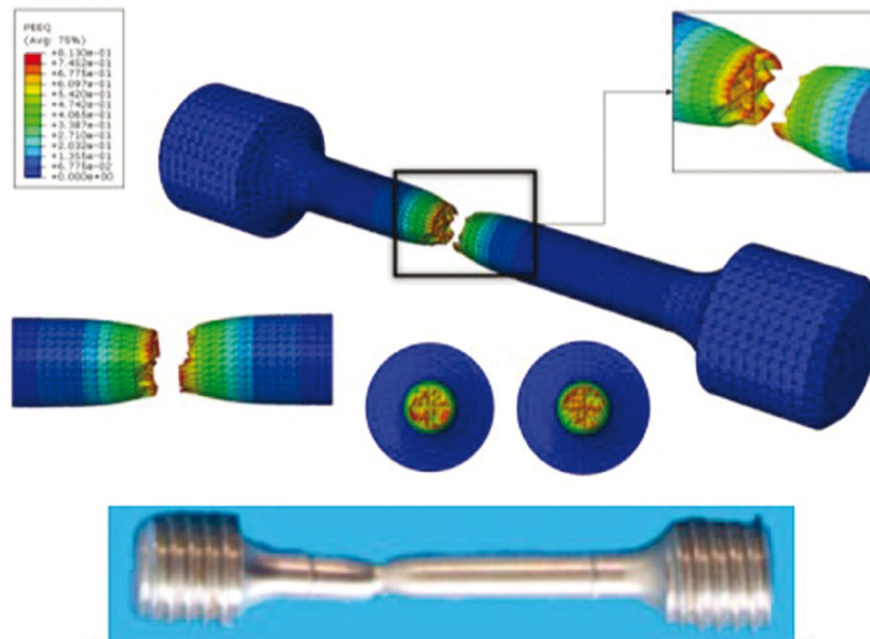$$\bar{\varepsilon}_f^p = C_3 \left(\frac{\sqrt{L^2+3}}{2} \right)^{C_1} \left[\frac{1}{1+C} \left(\bar{\eta} + \frac{3-L}{3\sqrt{L^2+3}} + C \right) \right]^{-C_2} \tag{3}$$

Where: $\bar{\eta}$ and $\bar{L}$ refer to the stress triaxiality and the Lode parameters averaged over the loading history which take account of the non-proportional loading effects, as expressed in Eq. (4) and Eq. (5). C is the cut-off value and is assumed to be 1/3 in this paper.

$$\bar{\eta} = \frac{1}{\bar{\varepsilon}_f^p} \int_0^{\bar{\varepsilon}_f^p} \eta \, d\bar{\varepsilon}^p \tag{4}$$

$$\bar{L} = \frac{1}{\bar{\varepsilon}_f^p} \int_0^{\bar{\varepsilon}_f^p} L \, d\bar{\varepsilon}^p \tag{5}$$

The stress triaxiality η and the Lode parameter L are given by:

$$\eta = \frac{\sigma_m}{\bar{\sigma}} = \frac{\sigma_1 + \sigma_2 + \sigma_3}{3\bar{\sigma}} \tag{6}$$

$$L = \frac{2\sigma_2 - \sigma_1 - \sigma_3}{\sigma_1 - \sigma_3} \tag{7}$$

Where: $\sigma_i (i = 1, 2, 3)$ is the principal stress.

As shown in Fig. 7, the fracture strain subject to uniaxial tension is determined to be 0.6975 based on the mes-

Fig. 8 Failure mode comparisons between FE simulation and physical test results [39]

H. Xin, J. Li, M. Veljkovic, Y. Liu, Q. Sun: Evaluating the strength of grade 10.9 bolts subject to multiaxial loading using the micromechanical failure index: MCEPS

ARTICLE
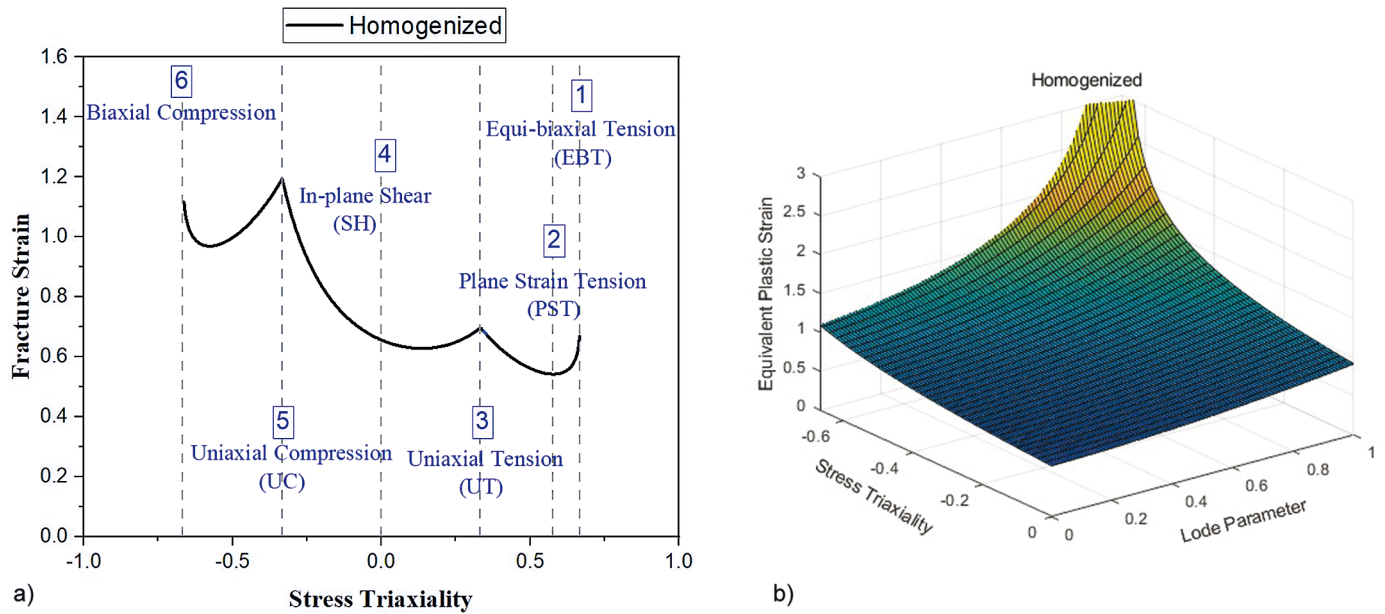
Fig. 9 Fracture locus of grade 10.9 bolts: a) fracture strain vs. stress triaxiality subject to plane stress status, b) fracture locus as a function of the stress triaxiality and Lode parameter

Fig. 10 Illustration and geometry of multiaxial loading set-up
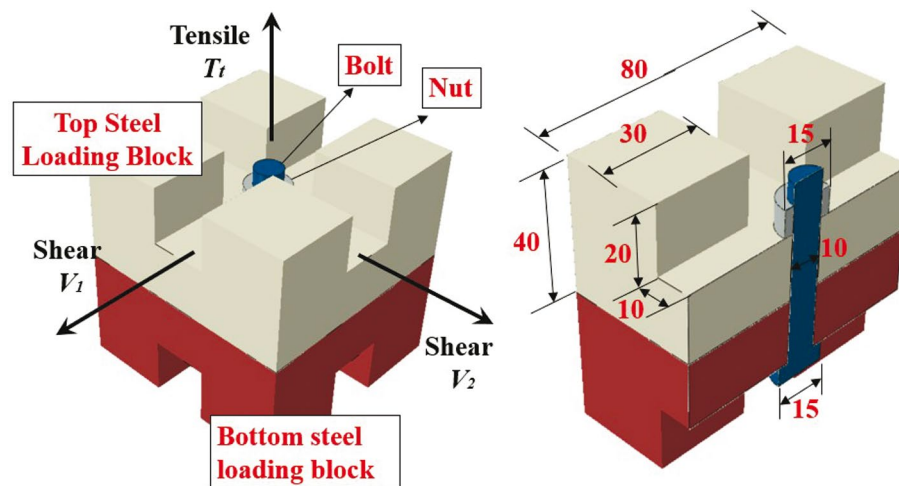
oscale failure index in which the FE simulation was consistent with the test results. The failure mode of the FE simulation is consistent with the experimental observations in [39], shown in the comparison in Fig. 8. The fracture locus based on the Lou-Huh model is shown in Fig. 9. The material parameters of fracture strains subject to uniaxial tension (UT), plane strain tension (PST), equal biaxial tension (EBT), in-plane shear (SH), uniaxial compression (UC), and equal biaxial compression (EBC) are listed in Tab. 3. The parameters of the fracture locus in Eq. (3) were determined as $C_1 = 1.45096$; $C_2 = 0.38814$ and $C_3 = 0.6975$.

3 Ultimate resistance of bolts subject to multiaxial loading

3.1 Finite element models

Bolted joints are generally subject to combined actions in steel structures applications, including combined tension load and shear actions (T_t-V_1), twin shear actions (V_1-V_2), and combined tension-twin shear actions (T_t-V_1-V_2). The loading set-up shown in Fig. 10 is used to apply different load combinations to the bolt shank. The diameter of the simplified bolt and nut model used in the simulation is

Tab. 3 Fracture strain at different stress status

$\bar{\varepsilon}^p_{EBT}$	$\bar{\varepsilon}^p_{PST}$	$\bar{\varepsilon}^p_{UT}$	$\bar{\varepsilon}^p_{SH}$	$\bar{\varepsilon}^p_{UC}$	$\bar{\varepsilon}^p_{EBC}$
0.6683	0.5425	0.6975	0.6564	1.1935	1.1167

Tab. 4 Summary of boundary conditions for multiaxial loading

Number	Step	RP1	RP2	RP3	RP4	RP5	RP6
ST	1				$Rot_{x,y,z}=0$ $U_{y,z}=0$ $F_x=P_{st}$	$Rot_{x,y,z}=0$ $U_{y,z}=0$	
	2	$Rot_{x,y,z}=0$ $U_y=0$	$Rot_{x,y,z}=0$ $U_{x,y,z}=0$	$Rot_{x,y,z}=0$ $U_{x,y,z}=0$	$Rot_{x,y,z}=0$ $U_y=0$ $F_x=P_{st}$	$Rot_{x,y,z}=0$ $U_y=0$ $U_z=8$ mm	$Rot_{x,y,z}=0$ $U_{x,y,z}=0$
	2				$Rot_{x,y,z}=0$ $U_y=0$ $F_x=0.9Vu$	$Rot_{x,y,z}=0$ $U_y=0$ $U_z=8$ mm	
SS	1	$Rot_{x,y,z}=0$ $U_{y,z}=0$	$Rot_{x,y,z}=0$ $U_{x,y,z}=0$	$Rot_{x,y,z}=0$ $U_{x,y,z}=0$	$Rot_{x,y,z}=0$ $U_{y,z}=0$ $F_x=P_{ss}$	$Rot_{x,y,z}=0$ $U_z=0$	$Rot_{x,y,z}=0$ $U_{x,y,z}=0$
	2	$Rot_{x,y,z}=0$ $U_z=0$ $U_y=8$ mm			$Rot_{x,y,z}=0$ $U_y=0$ $F_x=P_{ss}$		
SST	1	$Rot_{x,y,z}=0$ $U_y=0$	$Rot_{x,y,z}=0$ $U_{x,y,z}=0$	$Rot_{x,y,z}=0$ $U_{x,y,z}=0$	$Rot_{x,y,z}=0$ $U_y=0$ $F_x=P_{sst1}$	$Rot_{x,y,z}=0$ $U_y=0$ $F_x=P_{sst2}$	$Rot_{x,y,z}=0$ $U_{x,y,z}=0$
	2	$Rot_{x,y,z}=0$ $U_y=8$ mm			$Rot_{x,y,z}=0$ $F_x=P_{sst1}$	$Rot_{x,y,z}=0$ $F_x=P_{sst2}$	

Tab. 5 Summary of load values for multiaxial loading

Test number	P_{st}	P_{ss}	P_{sst1}	P_{sst2}
1	$0.0\ V_u$	$0.0\ V_u$	$0.2\ V_u$	$0.2\ V_u$
2	$0.2\ V_u$	$0.2\ V_u$	$0.2\ V_u$	$0.4\ V_u$
3	$0.4\ V_u$	$0.4\ V_u$	$0.2\ V_u$	$0.6\ V_u$
4	$0.6\ V_u$	$0.6\ V_u$	$0.2\ V_u$	$0.8\ V_u$
5	$0.8\ V_u$	$0.8\ V_u$	$0.4\ V_u$	$0.4\ V_u$
6	$0.9\ V_u$	$0.9\ V_u$	$0.4\ V_u$	$0.6\ V_u$
7			$0.4\ V_u$	$0.8\ V_u$
8			$0.6\ V_u$	$0.6\ V_u$
9			$0.6\ V_u$	$0.7\ V_u$

10 mm and 15 mm respectively. The parameters of the ductile fracture model detailed in Section 2 is used for the bolts during ultimate resistance evaluation. The total length, width and depth of the steel loading block is 80 mm, 80 mm and 40 mm respectively. A cross recess with a width of 20 mm is designed in the middle to settle the bolt. Elastic material properties are assigned to the steel loading block with elastic modulus 210.0 GPa and Poisson's ratio 0.3.

Different tensile and shear actions are applied to the steel loading block through reference points. The details of inter-
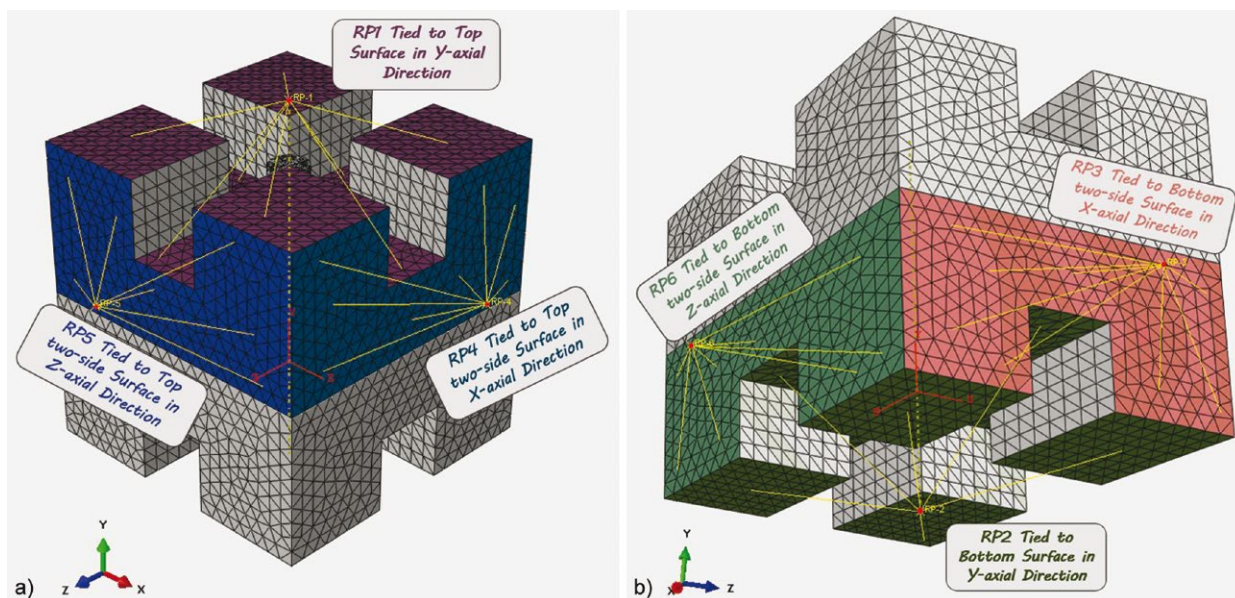
Fig. 11 FE model and boundary conditions of fitted bolt subject to multiaxial Loading specimen: a) view from the top, b) view from the below

H. Xin, J. Li, M. Veljkovic, Y. Liu, Q. Sun: Evaluating the strength of grade 10.9 bolts subject to multiaxial loading using the micromechanical failure index: MCEPS

ARTICLE

Tab. 6 Summary of ultimate resistance in different design standards

	Tensile	Shear	Combined tensile and shear	Multiaxial loading
GB 50017	$N_t^b = f_t^b A_s$	$N_v^b = A f_v^b$	$\left(\dfrac{F_{V,Ed}}{F_{V,Rd}}\right)^2 + \left(\dfrac{F_{t,Ed}}{F_{t,Rd}}\right)^2 \le 1.0$	$\left(\dfrac{F_{V1,Ed}}{F_{V1,Rd}}\right)^2 + \left(\dfrac{F_{V2,Ed}}{F_{V2,Rd}}\right)^2 + \left(\dfrac{F_{t,Ed}}{F_{t,Rd}}\right)^2 \le 1.0$
AISC-360	$\varphi R_n = \varphi F_{nt} A_b$	$\varphi R_n = \varphi F_{nv} A_b$	$\varphi R_n = \varphi F_{nt} A_b$ $\varphi R_n = \varphi F_{nv} A_b$	$\varphi R_n = \varphi F_{nt} A_b$ $\varphi R_n = \varphi F_{nv1} A_b$ $\varphi R_n = \varphi F_{nv2} A_b$
EN1993-1-8	$F_{t,Rd} = \dfrac{k_2 f_u^b A}{\gamma_{M2}}$	$F_{v,Rd} = \dfrac{\alpha_v f_u^b A}{\gamma_{M2}}$	$\dfrac{F_{V,Ed}}{F_{V,Rd}} + \dfrac{F_{t,Ed}}{1.4 F_{t,Rd}} \le 1.0$	$\dfrac{F_{V1,Ed}}{F_{V1,Rd}} + \dfrac{F_{V2,Ed}}{F_{V2,Rd}} + \dfrac{F_{t,Ed}}{1.4 F_{t,Rd}} \le 1.0$

Where: φ is the reduction factor, defined as 0.75 in this paper
A_b is the effective bolt area calculated according to the nominal diameter
γ_{M2} is the partial safety factor of ultimate resistance, defined as 1.25 in this paper
k_2 is the reduction factor, defined as 0.9
a_v is also the reduction factor, defined as 0.6
F'_{nt} is the corrected nominal tensile strength modified to include the influence of shear stress; can be determined as follows:

$$F'_{nt} = 1.3 F_{nt} - \frac{F_{nt}}{\varphi F_{nv}} f_{rv} \le F_{nt}$$

f_{rv} is the required shear stress using LRFD or ASD load combinations
F_{nt} is the nominal tensile stress
F'_{nv} is the corrected nominal shear strength (including the influence of tensile stress); can be determined as follows:

$$F'_{nv} = 1.3 F_{nv} - \frac{F_{nv}}{\varphi F_{nt}} f_{rt} \le F_{nv}$$

F_{nv} is the nominal shear stress
f_{rt} is the required tensile stress using LRFD or ASD load combinations.

actions between the reference points and the steel block are illustrated in Fig. 11. The boundary conditions and load values of the multiaxial loading are summarized in Tab. 4 and 5. A total of 21 models are calculated in this study.

3.2 Design recommendations

High-strength bolts up to grade 10.9 are covered by Chinese code GB 50017 [39], American code AISC-360 [41] and European code EN1993-1-8:2005 [42]. The ultimate resistance of bolts in different design standards is summarized in Tab. 6. Noted that the ultimate resistance subject to multiaxial loading has been extended to include the combined tensile and shear resistance equation.

3.3 Ultimate resistance of bolts under combined tensile and shear loading

Fig. 12 shows the failure modes under combined tensile and shear loading. In general, the bolts presented typical tensile-dominated failure when the shear force was zero. With increasing shear force, the failure mode changed to combined tensile-shear failure mode. The inclined angle of failure surface increased with increasing shear force values. Fig. 13 compares the ultimate capacity under combined shear and tensile loading of the numerical simulation with the design standards. Note that the experimental values of grade 10.9 bolts (M16, M20 and M24) under combined tension and shear actions reported in [11] is also illustrated in Fig. 13. The experimental results correlate

| $V_{u1}^* = 0.0 V_u$ | $V_{u1}^* = 0.2 V_u$ | $V_{u1}^* = 0.4 V_u$ | $V_{u1}^* = 0.6 V_u$ | $V_{u1}^* = 0.8 V_u$ |
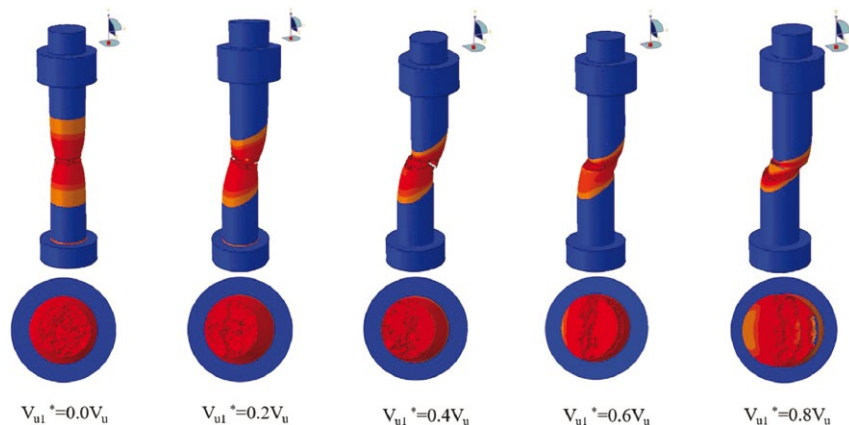
Fig. 12 Failure modes of bolts exposed to combined tensile and shear actions
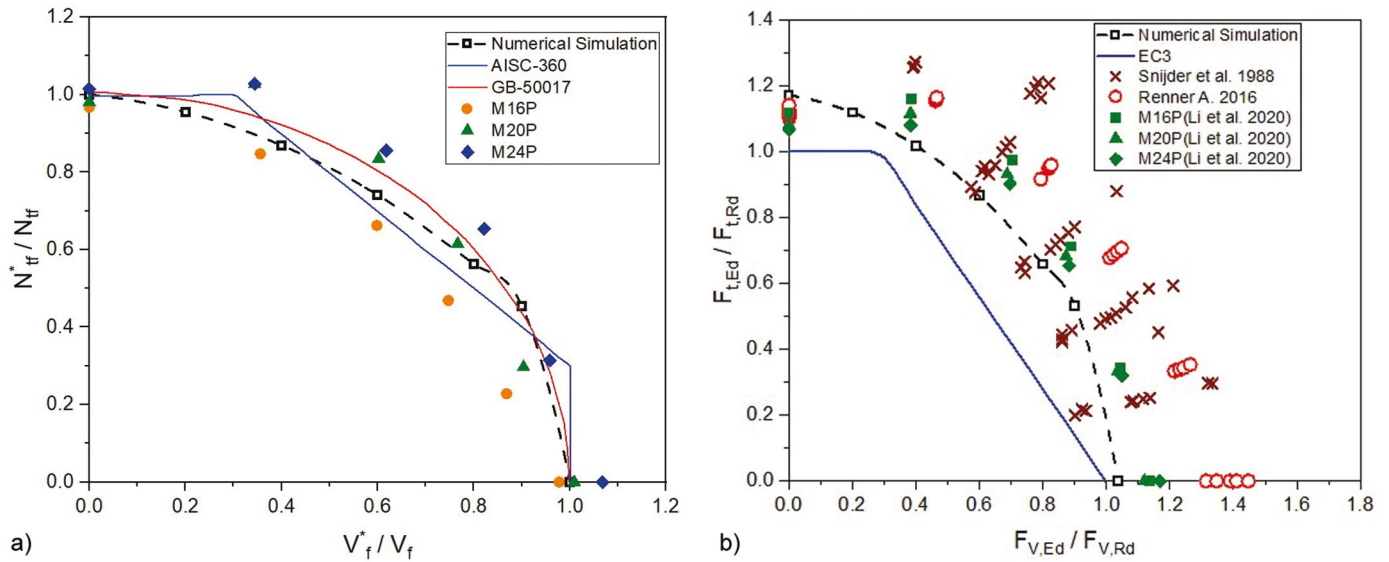
Fig. 13 Comparison between the ultimate capacity under combined tensile and shear actions of the numerical simulation and the design standards (the experimental observations are reproduced from [11, 43, 44]); a) comparisons between FE and Chinese/American Code, b) comparisons between FE and EN1993-1-8 results

well with the numerical simulations. Comparisons between the numerical simulations and Chinese code GB 50017 [39]/American code AISC-360 [41] in Fig. 13a show that predictions for the grade 10.9 bolt under combined tensile and shear loading were not on the safe side. In comparisons between the numerical simulation and European code EN1993-1-8 [42], the European code consistently provides conservative predictions for the bolt strength, especially under combined tensile and shear loading.
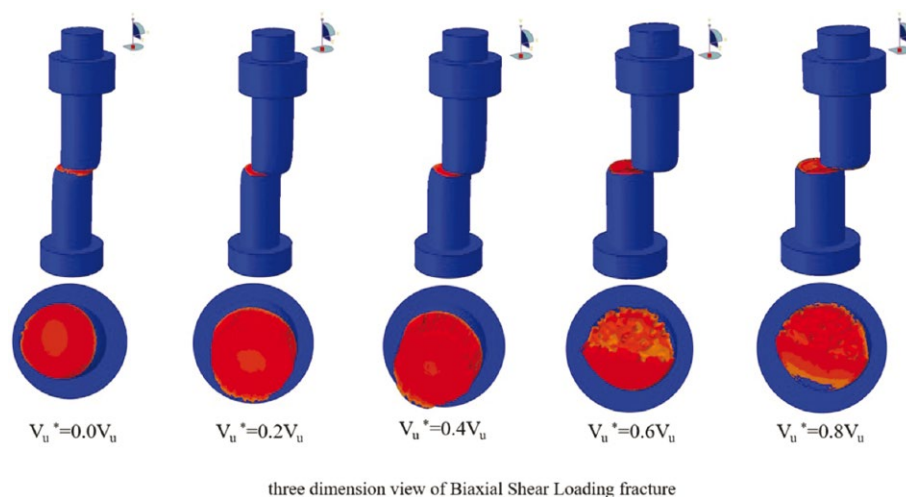
3.3 Ultimate resistance of bolts under biaxial shear loading

Fig. 14 shows the failure modes under twin shear loading. All the bolts presented a horizontal crack surface when under twin shear loading. The displacement in the other direction increased with increasing shear force values in other directions. Fig. 15 shows the ultimate resistance under twin shear loading of the numerical simulation in comparison with the design standards. Here too, predictions for the grade 10.9 bolt under twin shear loading were
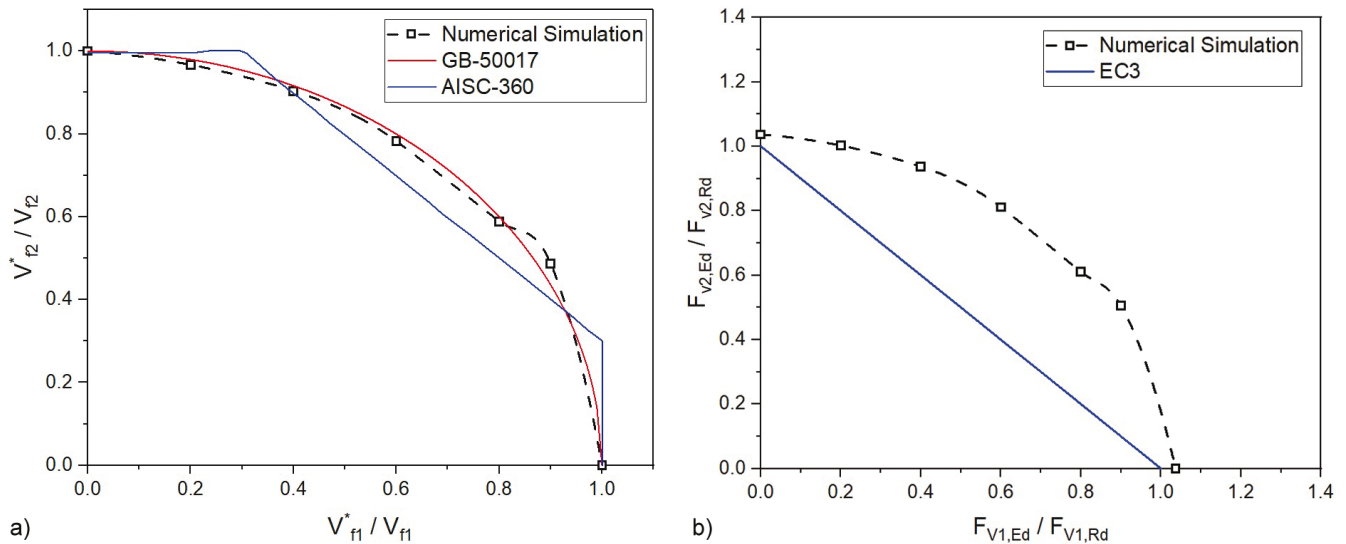
relatively unsafe in the comparisons between the numerical simulation and Chinese code GB 50017 [39]/American code AISC-360 [41], while in comparisons between the numerical simulation and European code EC3 [42], the European code EC3 [42] again gave conservative predictions for bolt strength, especially under twin shear loading.

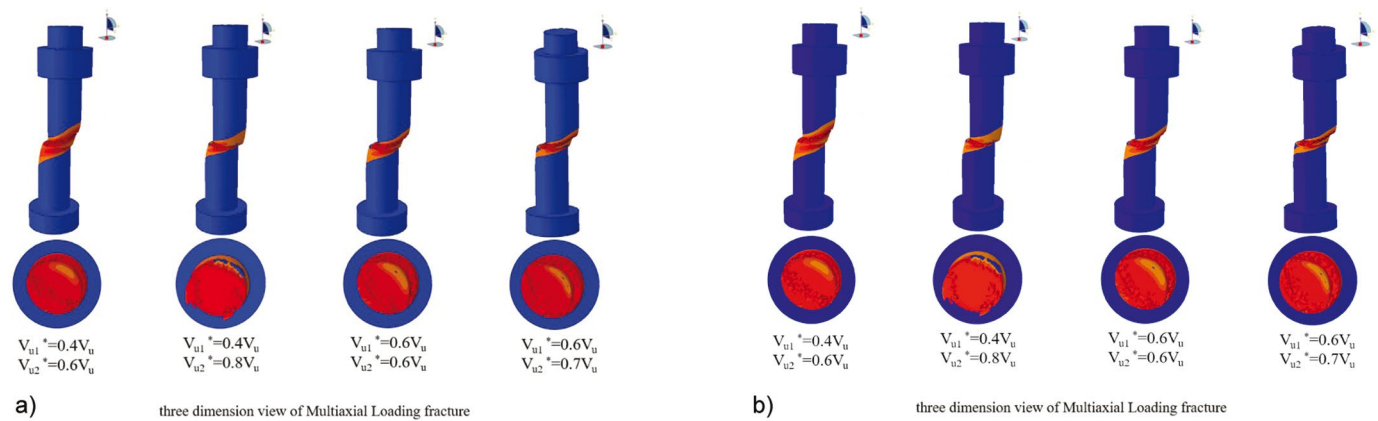### 3.4 Ultimate resistance of bolts under multiaxial loading

The failure modes under multiaxial loading are shown in Fig. 16. The failure mode changed to combined tensile-shear failure mode with increasing shear force value. Fig. 17 shows the ultimate resistance under multiaxial loading of the numerical simulation in comparison with the design standards. The results show that European code EN1993-1-8 [42] provides conservative predictions for bolt resistance under multiaxial loading compared with the numerical simulation. In the comparisons between the numerical simulation and Chinese code GB 50017 [39]/American code AISC-360 [41], the numerical resistance surface is covered by the resistance surface of


three dimension view of Biaxial Shear Loading fracture

Fig. 14 Failure modes of bolts subject to biaxial shear loading

H. Xin, J. Li, M. Veljkovic, Y. Liu, Q. Sun: Evaluating the strength of grade 10.9 bolts subject to multiaxial loading using the micromechanical failure index: MCEPS

ARTICLE

Fig. 15 Comparison between the ultimate resistance under twin shear actions of the numerical simulation and the design standards; a) comparisons between FE and Chinese/American Code, biaxial shear loading, b) comparisons between FE and EC3 Code

Fig. 16 Failure modes of bolts under tension-biaxial shear loading
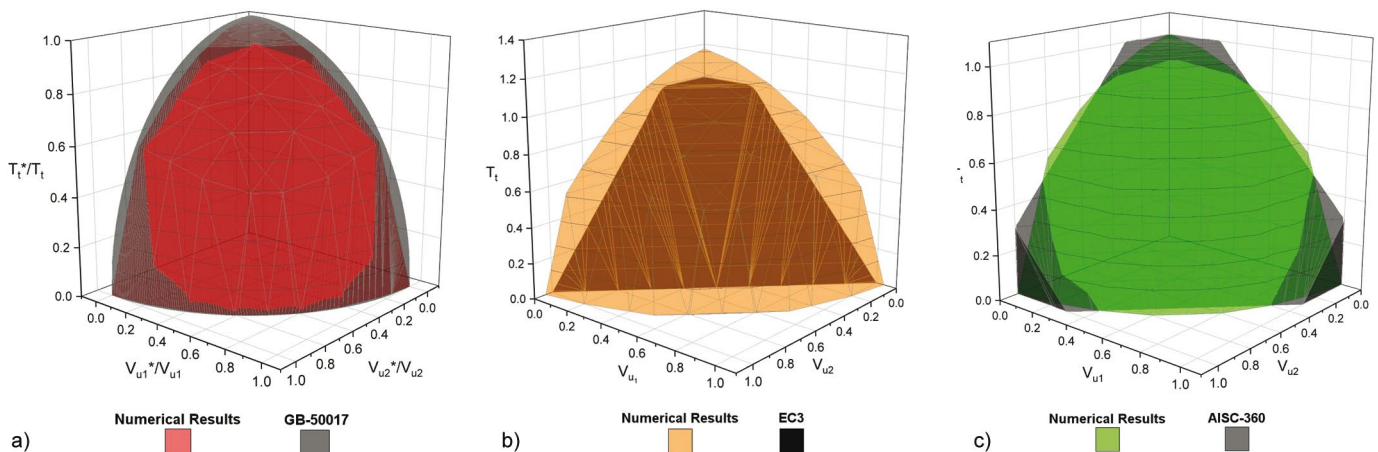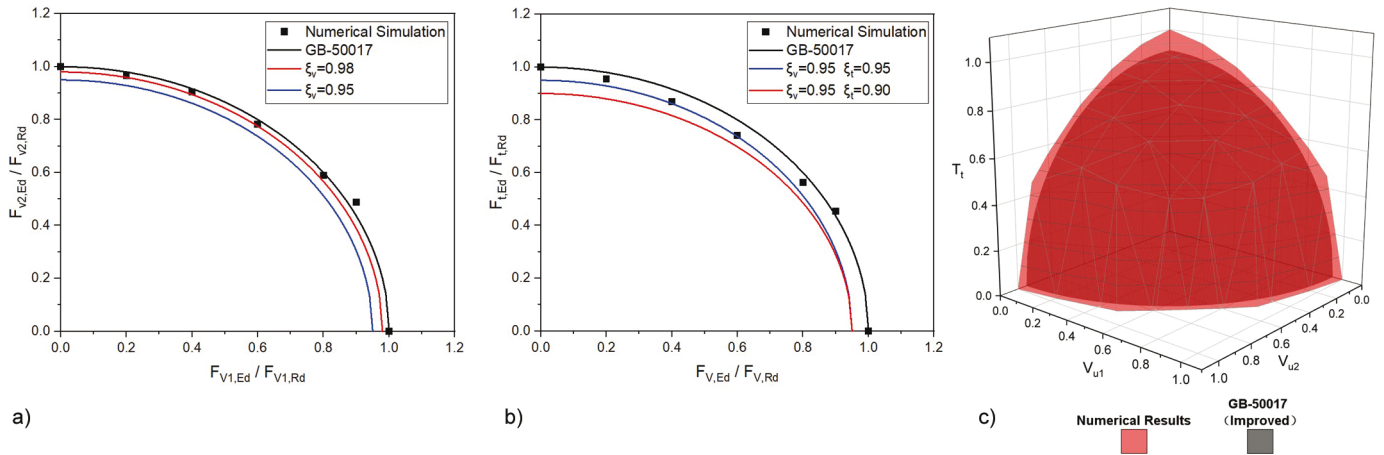

Fig. 17 Comparison between the ultimate capacity under multiaxial actions of the numerical simulation and the design standards; a) comparisons between FE and Chinese code, b) comparisons between FE and EC3 code, c) comparisons between FE and American code

the design standard close to the axis where one loading dominates, that means the predicted bearing capacity of bolts is greater than the value suggested from design specification. However, the design standards provide unsafe predictions when they are compared to FEA results for bolts under loading i.e. a middle area in Fig. 17a, c.

4   Discussion of the results

In this paper we considered the nominal values of bolt grade and geometry to investigate the most suitable prediction function to ensure the consistent safety of different load cases.

Fig. 18 Comparison between the ultimate resistance under multiaxial actions of the numerical simulation and the modified Chinese code; a) calibration of multi-axial loading factor for shear resistance ξ_v, b) calibration of multiaxial loading factor for tensile resistance ξ_t, c) comparisons between numerical simulation and design recommendations

4.1 Chinese design standard

Based on the comparison in Section 3, as expressed in Eq. (8), we proposed two modification factors, namely the multiaxial loading factor for shear resistance ξ_v and the multiaxial loading factor for tensile resistance ξ_t based on the design formula in Chinese code GB-50017. First, the ξ_v was calibrated based on the ultimate resistance of bolts under biaxial shear loading. We calculated ξ_v to be 0.95 as presented in Fig. 18a. Then the ξ_t was calibrated based on the ultimate resistance of bolts under combined tensile and shear loading. The ξ_t was also calculated to be 0.95 as shown in Fig. 18b. Comparison between the resistance under multiaxial actions of the numerical simulation and the modified GB-50017 is shown in Fig. 18c. The numerical resistance surface is enveloped by the resistance surface of design standard. In addition, the difference between the numerical resistance surface and the resistance surface of design standard is small, indicating validation of the calibrated parameters.

$$\left(\frac{F_{V1,Ed}}{\xi_v F_{V1,Rd}}\right)^2 + \left(\frac{F_{V2,Ed}}{\xi_v F_{V2,Rd}}\right)^2 + \left(\frac{F_{t,Ed}}{\xi_t F_{t,Rd}}\right)^2 \leq 1.0 \qquad (8)$$

4.2 European design standard

In this section we discuss the exponent and two modification factors ξ_v and ξ_t based on the comparison in Section 3, as expressed in Eq. (9). The exponent of EN1993-1-8:2005 is proposed as 1.0. As shown in Fig. 19, an exponent 1.0 is adopted to enable the simulated value to cover design recommendations in the three-dimensional figure. However, it produces a conservative prediction for combined tensile-shear actions, especially close to tensile-dominated ultimate resistance. When we compare the different exponents in Fig. 19, it is clear that exponent 2.0 give a better prediction in terms of overall trend. The exponent is proposed as 2.0, which is also consistent with Chinese and American design recommendations. The overestimation of shear-dominated ultimate resistance is revised by two modification factors ξ_v and ξ_t. Fig. 20
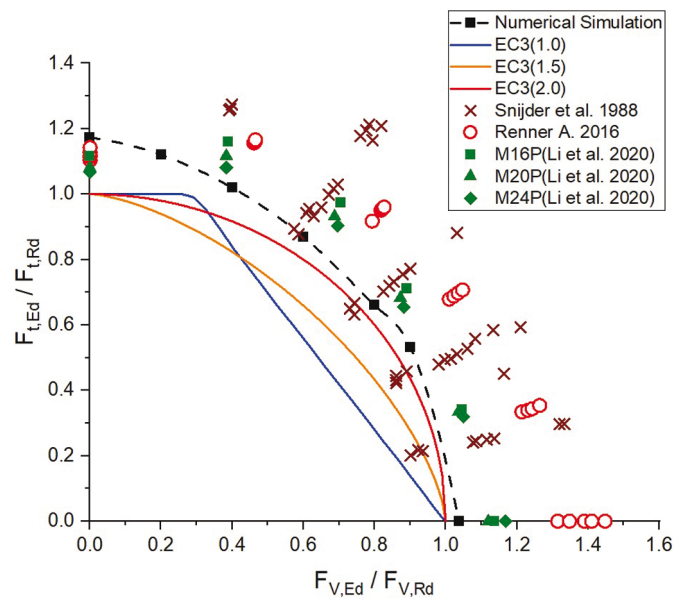
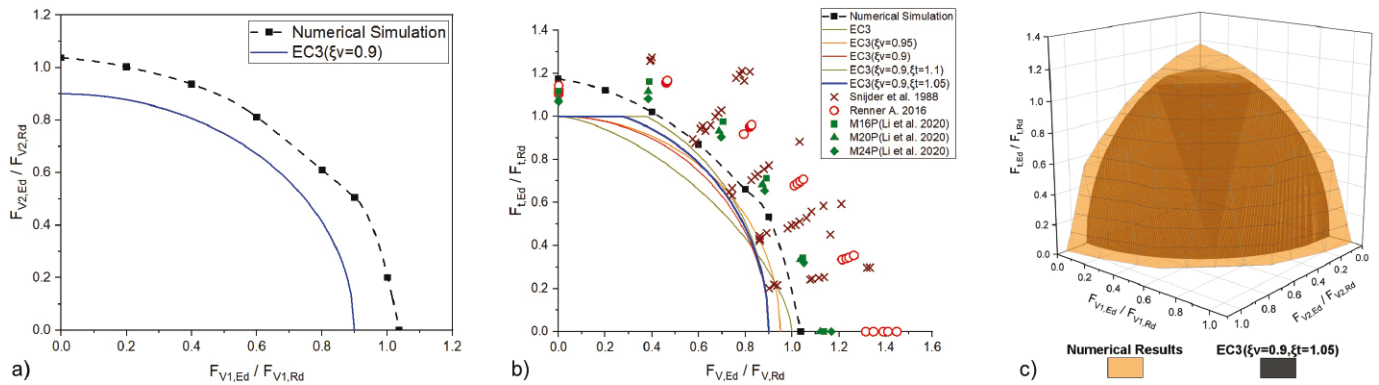**Fig. 19** Discussion of European code exponent

shows a comparison of the modified European code with the numerical/experimental results. We concluded that the better fits (where the prediction resistant function is more consistent with the experimental results) occurred when ξ_v is 0.90 and ξ_t is 1.05. The conservative prediction under combined uniaxial tension-biaxial shear loading from current recommendations in European code EN1993-1-8:2005 can be improved by using m = 2.0, ξ_v = 0.90 and ξ_t = 1.05 in Eq. (9).

$$\left(\frac{F_{V1,Ed}}{\xi_v F_{V1,Rd}}\right)^m + \left(\frac{F_{V2,Ed}}{\xi_v F_{V2,Rd}}\right)^m + \left(\frac{F_{t,Ed}}{\xi_t F_{t,Rd}}\right)^m \leq 1.0 \qquad (9)$$

5 Conclusions

Bolted connections are generally subject to combined actions, e.g. combined tension and shear actions, biaxial shear actions, and combined tension-biaxial shear actions. However, it is relatively difficult and time-consuming to conduct physical experiments in which multiaxial

H. Xin, J. Li, M. Veljkovic, Y. Liu, Q. Sun: Evaluating the strength of grade 10.9 bolts subject to multiaxial loading using the micromechanical failure index: MCEPS

ARTICLE

Fig. 20 Comparison between the ultimate resistance under multiaxial actions of the numerical simulation and the modified European code; a) calibration of multiaxial loading factor for shear resistance ξ_v, b) calibration of multiaxial loading factor for tensile resistance ξ_t, c) comparisons between numerical simulation and design recommendations

loading is applied to (high-strength) bolts. We calibrated the fracture locus of grade 10.9 bolts using the mesoscale critical equivalent plastic strain (MCEPS). Then we numerically evaluated the ultimate resistance of bolts under multiaxial loading using the ductile fracture simulation procedure. The following conclusions can be drawn:

1. The fracture strain under uniaxial tension was determined to be 0.6975 based on the mesoscale failure index in which the FE simulation was consistent with the test results. The fracture locus parameters were determined as $C_1 = 1.45096$; $C_2 = 0.38814$ and $C_3 = 0.6975$.
2. The ultimate bolt resistance subject to multiaxial loading was compared with current design standard. The results showed that predictions for the grade 10.9 bolt subject to multiaxial loading from Chinese code GB 50017 and American code AISC-360 are on the unsafe side while the European code EN1993-1-8:2005 provide a conservative prediction for bolt strength under multiaxial loading. It is worth mentioning that the same conclusion is valid even for the draft version of EN1993-1-8:2021.

3. We proposed two modification factors, namely multiaxial loading factor for shear resistance ξ_v and multiaxial loading factor for tensile resistance ξ_t based on Chinese code GB-50017 to better predict bolt strength under multiaxial loading. The ξ_v and ξ_t are 0.95 based on a short parametric study. After the modification, the complete numerical resistance surface is covered by the resistance surface of the design standard. In addition, the difference between the numerical resistance surface and the resistance surface of design standard is relatively small.
4. We also discussed the exponent and two modification factors ξ_v and ξ_t based on EN1993-1-8:2005 to improve the prediction of bolt strength under multiaxial loading. The better fits occurred when $m = 2.0$, $\xi_v = 0.90$ and $\xi_t = 1.05$. The conservative prediction, especially under uniaxial tension-biaxial shear actions, is improved compared with current recommendations of European code EN1993-1-8:2005.

References

[1] Chesson Jr, E.; Faustino, N. L.; Munse, W. H. (1965) *High-strength bolts subjected to tension and shear*. J Struct Div 91, No. ST5, pp. 155–180.
[2] Nair, R. S.; Birkemoe, P. C.; Munse, W. H (1974) *High strength bolts subject to tension and prying*. J Struct Div 100, pp. 351–372.
[3] Grimsmo, E. L.; Aalberg, A.; Langseth; M.; Clausen A. H. (2016) *Failure modes of bolt and nut assemblies under tensile loading*. J Constr Steel Res 126, pp. 15–25.
[4] Coelho, A. M. G; Bijlaard, F. S. K.; da Silva, L. S. (2004) *Experimental assessment of the ductility of extended end plate connections*. Eng Struct 26, pp. 1185–1206.
[5] Coelho, A. M. G; Bijlaard, F. S. K. (2007) *Experimental behaviour of high strength steel end-plate connections*. J Constr Steel Res 63, pp. 1228–1240.
[6] D'Aniello, M.; Cassiano, D.; Landolfo, R. (2016) *Monotonic and cyclic inelastic tensile response of European preloadable gr10.9 bolt assemblies*. J Constr Steel Res 124, pp. 77–90.
[7] Francavilla, A. B; Latour, M.; Piluso, V.; Rizzano, G. (2016) *Bolted T-stubs: A refined model for flange and bolt fracture modes*. Steel Compos Struct 20, pp. 267–293.

[8] Hedayat, A. A.; Afzadi, E. A.; Iranpour, A. (2017) *Prediction of the bolt fracture in shear using finite element method*. Structures 12, pp. 188–210.
[9] Hu, Y.; Shen, L.; Nie, S.; Yang, B.; Sha, W. (2016) *FE simulation and experimental tests of high-strength structural bolts under tension*. J Constr Steel Res 126, pp. 174–186.
[10] Guo, H.; Liang, G.; Li, Y.; Liu, Y. (2017) *Q690 high strength steel T-stub tensile behavior: Experimental research and theoretical analysis*. J Constr Steel Res 139, pp. 473–83.
[11] Li, D.; Uy, B.; Wang, J.; Song, Y. (2020) *Behaviour and design of Grade 10.9 high-strength bolts under combined actions*. Steel Compos Struct 35, pp. 327–41.
[12] Li, D.; Uy, B.; Wang, J.; Song, Y. (2020) *Behaviour and design of high-strength Grade 12.9 bolts under combined tension and shear*. J Constr Steel Res 174, pp. 106305.
[13] Song, Y.; Wang, J.; Uy, B.; Li, D. (2020) *Stainless steel bolts subjected to combined tension and shear: Behaviour and design*. J Constr Steel Res 170, pp. 106122.
[14] Benzerga, A. A.; Leblond, J.-B. (2010) *Ductile Fracture by Void Growth to Coalescence*. Adv Appl Mech 10, pp. 169–305.

[15] Weck, A.; Wilkinson, D. S. (2008) *Experimental investigation of void coalescence in metallic sheets containing laser drilled holes*. Acta Mater 56, pp. 1774–1784.

[16] McClintock, F. A. (1968) *A criterion for ductile fracture by the growth of holes*. Journal of Applied Mechanics, Transactions ASME 35, No. 2, pp. 363–371.

[17] Rice, J. R.; Tracey, D. M. (1969) *On the ductile enlargement of voids in triaxial stress fields*. J Mech Phys Solids 17, pp. 201–17.

[18] Gurson, A. L. (1977) *Continuum theory of ductile rupture by void nucleation and growth: Part I—Yield criteria and flow rules for porous ductile media*. Journal of Engineering Materials and Technology 99, pp. 2–15.

[19] Tvergaard, V. (1981) *Influence of voids on shear band instabilities under plane strain conditions*. Int J Fract 17, pp. 389–407.

[20] Tvergaard, V.; Needleman, A. (1984) *Analysis of the cup-cone fracture in a round tensile bar*. Acta Metall 32, pp. 157–69.

[21] Benzerga, A. A.; Besson, J. (2001) *Plastic potentials for anisotropic porous solids*. Eur J Mech 20, pp. 397–434.

[22] Nahshon, K.; Hutchinson, J. W. (2008) *Modification of the Gurson model for shear failure*. Eur J Mech A, Solids 27, p. 1.

[23] Xue, L. (2008) *Constitutive modeling of void shearing effect in ductile fracture of porous materials*. Eng Fract Mech 75, pp. 3343–3366.

[24] Mohr, D.; Marcadet, S. J. (2015) *Micromechanically-motivated phenomenological Hosford-Coulomb model for predicting ductile fracture initiation at low stress triaxialities*. Int J Solids Struct 67, pp. 40–55.

[25] Bai, Y.; Wierzbicki, T. (2008) *A new model of metal plasticity and fracture with pressure and Lode dependence*. Int J Plast 24, pp. 1071–96.

[26] Bao, Y.; Wierzbicki, T. (2004) *On fracture locus in the equivalent strain and stress triaxiality space*. Int J Mech Sci 46, pp. 81–98.

[27] Johnson, G. R.; Cook, W. H. (1983) *A constitutive model and data for metals subjected to large strains, high strain rates and high temperatures*. Proc. 7th Int. Symp. Ballist., Vol. 21, The Netherlands, pp. 541–547.

[28] Bai, Y.; Wierzbicki, T. (2010) *Application of extended Mohr-Coulomb criterion to ductile fracture*. Int J Fract 161, p. 1.

[29] Roth, C. C.; Mohr, D. (2014) *Effect of strain rate on ductile fracture initiation in advanced high strength steel sheets: Experiments and modeling*. Int J Plast 56, pp. 19–44.

[30] Marcadet, S. J.; Mohr, D. (2015) *Effect of compression-tension loading reversal on the strain to fracture of dual phase steel sheets*. Int J Plast 72, pp. 21–43.

[31] Lou, Y.; Yoon, J. W.; Huh, H. (2014) *Modeling of shear ductile fracture considering a changeable cut-off value for stress triaxiality*. Int J Plast 54, pp. 56–80.

[32] Lou, Y.; Huh, H.; Lim, S.; Pack, K. (2012) *New ductile fracture criterion for prediction of fracture forming limit diagrams of sheet metals*. Int J Solids Struct 49, pp. 3605–3615.

[33] Cao, T. S. (2017) *Models for ductile damage and fracture prediction in cold bulk metal forming processes: a review*. Int J Mater Form 10, pp. 139–171.

[34] Chaboche, J.-L. (1984) *Anisotropic creep damage in the framework of continuum damage mechanics*. Nucl Eng Des 79, pp. 309–319.

[35] Lemaitre, J. (1986) *Local approach of fracture*. Eng Fract Mech 25, pp. 523–537.

[36] Lemaitre, J.; Desmorat, R. (2005) *Engineering damage mechanics: ductile, creep, fatigue and brittle failures*. Berlin, Heidelberg: Springer.

[37] Xin, H.; Correia, J. A. F. O.; Veljkovic, M.; Berto, F. (2021) *Fracture parameters calibration and validation for the high strength steel based on the mesoscale failure index*. Theor Appl Fract Mech 112, pp. 102929.

[38] Xin, H.; Veljkovic, M; José, A. F. O.; Correia, Berto, F. (2021) *Ductile fracture locus identification using mesoscale critical equivalent plastic strain*. Fatigue Fract Eng Mater Struct 44, pp. 1292–1304.

[39] GB 50017-2003 (2003) *Code for design of steel structures Beijing*. China Architecture & Building Press [in Chinese].

[40] Xin, H; Veljković, M. (2021) *Evaluation of High Strength Steels Fracture Based on Uniaxial Stress-Strain Curves*. Eng Fail Anal 120, pp. 105025.

[41] AISC 360-05 (2005) *Specification for Structural Steel Buildings*. American Institute of Steel Construction, Inc., Chicago, IL.

[42] 1993-1-1 EN (2005) *Eurocode 3: Design of steel structures: General rules and rules for buildings*.

[43] Snijder, H. H.; Ungermann, D.; Stark, J. W. B.; Sedlacek, G.; Bijlaard, F. S. K.; Hemmert-Halswick, A. (1988) *Evaluation of test results on bolted connections in order to obtain strength functions and suitable model factors – Part B: Evaluations*. Eurocode 3 Editorial Group, 1988.

[44] Renner, A. (2016) *Zug-Abscher-Interaktion bei Schrauben im Stahlbau* [Dissertation]. TU Darmstadt.

Authors

Prof. Haohui Xin (corresponding author)
xinhaohui@xjtu.edu.cn
Xi'an Jiaotong University
Department of Civil Engineering, School of Human Settlements and Civil Engineering
No.28, West Xianning Road
Xi'an, Shaanxi, 710049, P.R. China

Jie Li
Xi'an Jiaotong University
Department of Civil Engineering, School of Human Settlements and Civil Engineering
No.28, West Xianning Road
Xi'an, Shaanxi, 710049, P.R. China

Prof. Milan Veljkovic
Delft University of Technology
Faculty of Civil Engineering and Geosciences
Building 23, Stevinweg 1 / PO box 5048
2628 CN Delft, Netherlands

Prof. Yuqing Liu
Tongji University
Department of Bridge Engineering
1239 Siping Road
Shanghai, 200092, P.R. China

Prof. Qing Sun
Xi'an Jiaotong University
Department of Civil Engineering, School of Human Settlements and Civil Engineering
No.28, West Xianning Road
Xi'an, Shaanxi, 710049, P.R. China

How to Cite this Paper